A&A 608, A56 (2017)
DOI: 10.1051/0004-6361/201731862

Astronomy & Astrophysics

ALMA imaging of C_2H emission in the disk of NGC 1068

S. García-Burillo[1], S. Viti[2], F. Combes[3], A. Fuente[1], A. Usero[1], L. K. Hunt[4], S. Martín[5,6], M. Krips[7], S. Aalto[8], R. Aladro[8,9], C. Ramos Almeida[10,11], A. Alonso-Herrero[12], V. Casasola[4], C. Henkel[9,13], M. Querejeta[1,14], R. Neri[7], F. Costagliola[8], L. J. Tacconi[15], and P. P. van der Werf[16]

(Affiliations can be found after the references)

Received 30 August 2017 / Accepted 18 September 2017

ABSTRACT

Aims. We study the feedback of star formation and nuclear activity on the chemistry of molecular gas in NGC 1068, a nearby (D = 14 Mpc) Seyfert 2 barred galaxy, by analyzing whether the abundances of key molecular species such as ethynyl (C_2H), which is a classical tracer of photon dominated regions (PDR), change in the different environments of the disk of the galaxy.

Methods. We used the Atacama Large Millimeter Array (ALMA) to map the emission of the hyperfine multiplet of $C_2H(N = 1-0)$ and its underlying continuum emission in the central $r \simeq 35''$ (2.5 kpc) region of the disk of NGC 1068 with a spatial resolution $1\farcs0 \times 0\farcs7$ (≃50−70 pc). We used maps of the dust continuum emission obtained at 349 GHz by ALMA to derive the H_2 gas column densities and combined these with the C_2H map at matched spatial resolution to estimate the fractional abundance of this species. We developed a set of time-dependent chemical models, which include shocks, gas-phase PDRs, and gas-grain chemical models to determine the origin of the C_2H gas.

Results. A sizeable fraction of the total C_2H line emission is detected from the $r \simeq 1.3$ kpc starburst (SB) ring, which is a region that concentrates the bulk of the recent massive star formation in the disk traced by the Paα emission complexes imaged by the *Hubble* Space Telescope (HST). However, the brightest C_2H emission originates from a $r \simeq 200$ pc off-centered circumnuclear disk (CND), where evidence of a molecular outflow has been previously found in other molecular tracers imaged by ALMA. We also detect significant emission that connects the CND with the outer disk in a region that probes the interface between the molecular disk and ionized gas outflow out to $r \simeq 400$ pc. We derived the fractional abundances of C_2H ($X(C_2H)$) assuming local thermodynamic equilibrium (LTE) conditions and a set of excitation temperatures (T_{ex}) constrained by the previous multiline CO studies of the galaxy. Our estimates range from $X(C_2H) \simeq$ a few 10^{-8} in the SB ring up to $X(C_2H) \simeq$ a few 10^{-7} in the outflow region. The PDR models that incorporate gas-grain chemistry are able to account for $X(C_2H)$ in the SB ring for moderately dense ($n(H_2) \geq 10^4$ cm^{-3}) and moderately UV-irradiated gas (UV-field ≤ 10 × Draine field, where 1 Draine field ≡ 2.74×10^{-3} erg s^{-1} cm^{-2}) in a steady-state regime, which depending on the initial and physical conditions of the gas may be achieved by 10^5 yr or as late as 10^7 yr. However, the high fractional abundances estimated for C_2H in the outflow region can only be reached at very early times ($T \leq 10^{2-3}$ yr) in models of UV or X-ray irradiated dense gas ($n(H_2) \geq 10^{4-5}$ cm^{-3}).

Conclusions. We find that the transient conditions required to fit the high values of $X(C_2H)$ in the outflow are likely due to UV or X-ray irradiated non-dissociative shocks associated with the highly turbulent interface between the outflow and molecular gas in NGC 1068. Although the inferred local timescales are short, the erosion of molecular clouds by the active galactic nucleus (AGN) wind and/or the jet likely resupplies the interface working surface continuously, making a nearly steady state persist in the disk of the galaxy.

Key words. galaxies: individual: NGC 1068 – galaxies: ISM – galaxies: kinematics and dynamics – galaxies: nuclei – galaxies: Seyfert – radio lines: galaxies

1. Introduction

Multiline observations of different molecular tracers can probe the feedback of star formation and/or nuclear activity on the chemistry and energy balance of the interstellar medium of galaxies. There is mounting observational evidence suggesting that the excitation and chemistry of the main molecular species in active galactic nuclei (AGN) are different with respect to those found in purely star-forming galaxies ("starbursts", SBs) (e.g., Tacconi et al. 1994; Kohno et al. 2001; Usero et al. 2004; Martín et al. 2006; Krips et al. 2008; Aladro et al. 2011, 2013; Imanishi & Nakanishi 2013). Recent progress in the capabilities of millimeter and submillimeter telescopes has made a large set of molecular line transitions from various species, beyond CO line studies, detectable in the nearest sources. These observations can be used to analyze the physical and chemical properties of the different gas components within a galaxy along with its dominant energetics.

The C_2H (ethynyl) multiplet at 3 mm has a critical density of 2×10^5 cm^{-3} at T_k = 100 K (not including radiative trapping effects) and hence traces relatively dense gas. However, as for other molecular transitions (e.g., Shirley 2015), the effective excitation density of the C_2H multiplet, which is defined as that producing emission strong enough to be observed (above a ∼1 K km s^{-1} detection threshold in Shirley's study), can be up to a factor of 10 lower. The emission of C_2H has been detected in a wide variety of molecular cloud environments in our Galaxy from dense Galactic cores ($n(H_2) \geq 10^{5-6}$ cm^{-3}) to more diffuse clouds ($n(H_2) \leq 10^{4-5}$ cm^{-3}). In the early studies of Galactic molecular clouds the abundances of ethynyl, defined as $X(C_2H) \equiv N(C_2H)/N(H_2)$, were seen to increase from dense gas, where $X(C_2H) \simeq (1-60) \times 10^{-10}$ (Wootten et al. 1980; Huggins et al. 1984; Watt 1983; Watt et al. 1988), to diffuse and translucent gas clouds, where $X(C_2H) \simeq 2 \times 10^{-8}$ (Turner et al. 1999). The reason behind this trend is that in diffuse molecular gas CO can be more easily dissociated by UV photons. This process releases carbon for C_2H formation and increases the abundance of this species in the gas phase, as predicted by stationary-state chemical models (e.g., Sternberg & Dalgarno 1995).

Because of the key role of UV photons, the chemistry of C_2H is generally linked to ionized carbon, so that its abundance is a good tracer of the UV-pervaded outer boundary ($A_V = 1-5^m$) of

Galactic molecular clouds, known as photon dominated regions (PDR), where $X(C_2H) \geq 10^{-8}$ (Fuente et al. 1993; Pety et al. 2005; Beuther et al. 2008; Walsh et al. 2010; Pilleri et al. 2013; Cuadrado et al. 2015). The changes in ethynyl abundances have also been interpreted in terms of chemical evolution in time-dependent models, where chemically younger regions at lower densities would favor higher abundances of C_2H (Li et al. 2012; Pan et al. 2017). Alternatively, Bayet et al. (2011b,a), showed that C_2H can be a tracer of regions influenced by the dissipation of turbulence and waves, heating the gas and accelerating cosmic rays.

The abundance of C_2H has also been found to be comparable to that of molecular species, such as HCN or HCO^+, in a wide variety of external galaxies, i.e., $X(C_2H) \geq 10^{-9}-10^{-8}$. These extragalactic observations include SBs (Henkel et al. 1988; Wang et al. 2004; Meier & Turner 2005; Martín et al. 2006; Aladro et al. 2011; Nakajima et al. 2011; Meier & Turner 2012; Meier et al. 2015), AGNs (Bayet et al. 2011a; Nakajima et al. 2011; Aladro et al. 2013; Martín et al. 2015), low-metallicity objects (Heikkilä et al. 1999), ultraluminous infrared galaxies (ULIRGs; Costagliola et al. 2011) and isolated normal galaxies (Martín et al. 2014). Although the detection of significant C_2H emission in galaxies has been generally linked to PDR chemistry in star-forming regions, other scenarios that point more specifically to outflow-driven chemistry could provide an alternative explanation to the detection of ethynyl in the molecular outflow of Maffei 2 published by Meier & Turner (2012).

NGC 1068 is a prototypical nearby ($D \simeq 14$ Mpc) Seyfert 2 galaxy, which has been the subject of numerous observational campaigns conducted with single-dish telescopes devoted to studying the fueling of its central region and related feedback using molecular line observations (e.g., Usero et al. 2004; Israel 2009; Kamenetzky et al. 2011; Hailey-Dunsheath et al. 2012; Aladro et al. 2013). NGC 1068 is an archetype of a composite SB/AGN galaxy. High-resolution observations of CO, and of more specific tracers of dense gas such as HCN, HCO^+, CS, and SiO, have proved that interferometers are needed to disentangle the SB/AGN components in the circumnuclear region of this galaxy by spatially resolving the distribution, kinematics, and excitation of molecular gas (Tacconi et al. 1994; Schinnerer et al. 2000; García-Burillo et al. 2010; Krips et al. 2011; García-Burillo et al. 2014, 2016; Takano et al. 2014; Nakajima et al. 2015; Imanishi et al. 2016; Gallimore et al. 2016).

García-Burillo et al. (2014) used the Atacama Large Millimeter Array (ALMA) to map the emission of a set of dense molecular gas tracers (CO(3–2), CO(6–5), HCN(4−3), HCO^+(4−3), and CS(7–6)) in the central $r \sim 2$ kpc of NGC 1068 with spatial resolutions $\simeq$0.3″−0.5″ (20–35 pc). The CO(3–2) line emission in the ALMA map stems from three regions: 1) the circumnuclear disk (CND); 2) the bar; and 3) the SB ring. Most of the CO(3–2) flux in the ALMA map of García-Burillo et al. (2014) comes from the SB ring, which is a two-armed spiral structure that starts from the ends of the stellar bar and forms a molecular gas pseudo-ring at $r \sim 18''$ (∼1.3 kpc). The SB ring concentrates the bulk of the massive star formation in the galaxy. The CND is an elliptical ring of 350 pc diameter that is off-centered relative to the AGN. In the immediate vicinity of the CND, the CO(3–2) emission is detected in an arc-like component on the northeastern side of the disk at distances $r \simeq 5-6''$ (400 pc) from the AGN. The anomalous velocities measured both in the arc feature and the CND reveal an AGN-driven massive molecular outflow. García-Burillo et al. (2014) concluded that the molecular outflow is launched when the ionization cone of the narrow line region (NLR) sweeps the disk in the CND and further to the north in the bow-shock arc. More recently, ALMA observations of the CND in the CO(6−5), HCN(3–2), and HCO^+(3−2) lines, carried out with spatial resolutions $\simeq$4−10 pc, have been able to isolate and image the dust continuum and molecular line emission from a $\simeq$7−10 pc–diameter disk, which represents the submillimeter counterpart of the putative AGN torus of this galaxy (García-Burillo et al. 2016; Imanishi et al. 2016; Gallimore et al. 2016).

Molecular line ratios analyzed by García-Burillo et al. (2014) and Viti et al. (2014) are significantly different in the SB ring and the CND. The change in molecular line ratios inside the CND indicate that radiative and mechanical feedback from the AGN has dramatically changed the physical conditions of molecular gas and chemical abundances of some molecular species in the outflow region (see also Kelly et al. 2017). The SB ring is colder and less dense than the CND and there are also differences in their chemistry (Viti et al. 2014).

The emission of the C_2H multiplet in the disk of NGC 1068 was first observed by Costagliola et al. (2011) and Aladro et al. (2013) with the IRAM 30 m single-dish telescope. In particular, Aladro et al. (2013) used a chemical model to reproduce the average C_2H abundances derived from their data but they were not able to discern whether the C_2H emission was arising from PDRs, dense or shocked gas owing to the insufficient spatial resolution of these single-dish observations ($\simeq$29″). In this work we use the unique high spatial resolution ($\leq$1″) and sensitivity capabilities of ALMA to image the emission of C_2H in the different environments of the NGC 1068 disk. We also use a set of newly developed shock models, gas-phase PDR models, and gas-grain chemical models to account for the abundances derived for C_2H.

Hereafter we assume a distance to NGC 1068 of $D \simeq 14$ Mpc (Bland-Hawthorn et al. 1997); the latter implies a spatial scale of $\simeq$70 pc/″.

2. Observations

2.1. ALMA data

We observed the emission of the hyperfine multiplet of C_2H(N = 1−0) in the central $r \simeq 35''$ (2.5 kpc) region of the disk of NGC 1068 with ALMA during Cycle 2 (project-ID: #2013.1.00055.S; PI: S. García-Burillo). We used Band 3 receivers and a single pointing. We observed one track in August 2015 with 34 antennas with projected baselines ranging from 12 m to 1430 m. The phase tracking center was set to $\alpha_{2000} = 02^h42^m40.771^s$, $\delta_{2000} = -00°00'47.84''$, which is the center of the galaxy according to SIMBAD taken from the Two Micron All Sky Survey – 2MASS survey (Skrutskie et al. 2006). The tracking center is offset by $\leq$1″ relative to the AGN position, $\alpha_{2000} = 02^h42^m40.71^s$, $\delta_{2000} = -00°00'47.94''$ (Gallimore et al. 1996, 2004, 2016; García-Burillo et al. 2014, 2016; Imanishi et al. 2016). The CND and the SB ring of NGC 1068 are both located inside the central $r \simeq 25''$(1.8 kpc) of the disk, i.e., well inside the field of view of the 70″ FWHM primary beam of the single-pointed observations.

We used four spectral windows each with a bandwidth of 1.875 GHz and a spectral resolution of $\simeq$0.98 MHz (3.4 km s^{-1}). Two of these windows were placed in the lower side band (LSB) and the other two in the upper sideband (USB). The lowest frequency window of the LSB was centered on the sky frequency 86.3082 GHz. This setup allowed us to observe the whole hyperfine set of lines of C_2H. The C_2H (N = 1−0) multiplet, hereafter referred to as C_2H (1−0), comprises six hyperfine components grouped in two fine structure groups denoted as

Table 1. Line components of the $C_2H(N = 1-0)$ multiplet.

Fine structure group	Hyperfine structure line	Frequency (GHz)	Line strength (S_{ij})
Group-I	$J = 3/2 - 1/2$, $F = 1-1$	87.284	0.17
Group-I	$J = 3/2 - 1/2$, $F = 2-1$	87.317	1.67
Group-I	$J = 3/2 - 1/2$, $F = 1-0$	87.329	0.83
Group-II	$J = 1/2 - 1/2$, $F = 1-1$	87.402	0.83
Group-II	$J = 1/2 - 1/2$, $F = 0-1$	87.407	0.33
Group-II	$J = 1/2 - 1/2$, $F = 1-0$	87.447	0.17

Notes. Frequencies taken from the Cologne Database for Molecular Spectroscopy (CDMS; Endres et al. 2016).

group-I and group-II in Table 1. For the typical linewidths observed in NGC 1068 we can resolve the two fine groups in velocity, but not the lines they consist of. If the opacity of the lines is low, we expect that the strongest hyperfine component corresponds to $J = 3/2-1/2$, $F = 2-1$ at $\nu = 87.317$ GHz (rest frequency). We therefore take this frequency as the reference for the velocity scale, which is hereafter derived relative to $v_{\rm sys}^{\rm HEL} = 1136$ km s^{-1} (García-Burillo et al. 2016).

We calibrated the data via the ALMA reduction package CASA[1]. The calibrated uv tables were transformed to GILDAS[2]-readable format where the mapping and cleaning were performed. The angular resolution obtained using natural weighting was $1\farcs0 \times 0\farcs7$ (70 pc × 50 pc) at a position angle PA = 69° in the line and continuum data cubes. The conversion factor between Jy beam^{-1} and K is 240 K Jy^{-1} beam. The line data cube was binned to a frequency resolution of ≃2.92 MHz (≃10 km s^{-1}). The estimated 1σ rms in the line data cube, derived in line-free emission areas, is ≃0.4 mJy beam^{-1} in ≃10 km s^{-1} channels. An image of the continuum emission at a mean frequency of 86.3 GHz was obtained by averaging 60 channels (≃600 km s^{-1}) free of line emission around the C_2H. The corresponding point source sensitivity for the continuum is 80 μJy beam^{-1}. All the maps were corrected for the attenuation by the primary beam, assuming a FWHM of 70″ for the latter. We estimate that the absolute flux accuracy in the maps is about 10–15%.

As our observations do not contain short-spacing correction, we expect to start filtering out an increasing fraction of the line and continuum emissions on scales >4″; the latter corresponds to the expected largest angular scale of the emission that can be recovered in the ALMA maps used in this work. This likely affects the faint emission that extends on large scales in the inter-arm region. Costagliola et al. (2011) measured in NGC 1068 an integrated flux for the C_2H multiplet of $T_a^*\Delta v \simeq 8 \pm 2$ K km s^{-1} (47 ± 12 Jy km s^{-1}) inside the 29″ IRAM-30 m telescope beam at 86.3 GHz. This is similar to the flux estimated by Aladro et al. (2013), i.e., ≃7 K km s^{-1}. The corresponding flux measured by ALMA for the same aperture is ≃35 ± 5 Jy km s^{-1}, which is ≃75–85% of the 30 m flux estimates. The clumpiness of the C_2H-emitting gas that we observe in the SB ring and the CND, aided by the velocity structure of the emission, explains why we recover with ALMA most of the total C_2H flux over these regions. This scenario has been also tested for other molecular gas tracers mapped by ALMA in NGC 1068 (García-Burillo et al. 2014; Tosaki et al. 2017).

[1] http//casa.nrao.edu/
[2] http://www.iram.fr/IRAMFR/GILDAS

2.2. Ancillary data

We retrieved the HST NICMOS (NIC3) narrowband (F187N, F190N) data of NGC 1068 from the *Hubble* Legacy Archive (HLA) to obtain calibrated images for the Paα line emission. These images were completely reprocessed with a calibration pipeline as explained in detail in Sect. 2.2 of García-Burillo et al. (2014). The pixel size of the HLA images is 0″.1 square.

We also use the CO(3–2) line and continuum maps of NGC 1068 obtained with ALMA during Cycle 0 using Band 7 receivers (project-ID: #2011.0.00083.S; PI: S. García-Burillo) and published by García-Burillo et al. (2014) and Viti et al. (2014).

3. Results

3.1. Continuum map

Figure 1 shows the continuum map derived at 86.3 GHz in NGC 1068. The bulk of the continuum emission stems from a highly structured elongated jet-like feature that emanates from the nucleus and extends out to $r \simeq 9''$ along PA $\simeq 30°$ [3]. The emission comprises several components that are similar to those imaged in the high-resolution radio continuum maps of the galaxy obtained at cm wavelengths (Wilson & Ulvestad 1983, 1987; Ulvestad et al. 1987; Gallimore et al. 1996, 2004).

The brightest emission corresponds to an elongated nuclear spot close to the AGN. The nuclear spot was spatially resolved into a quadruple source in the previous subarcsecond radio continuum maps of Gallimore et al. (1996, 2004): this includes the source S1, identified as the AGN core, and sources S2, C, and NE, which are forming the inner section of a collimated jet that emits synchrotron emission. A similar elongated feature was identified by Imanishi et al. (2016) in their 1.1 mm (266 GHz) continuum map obtained with ALMA.

On larger scales, we detected emission to the southwest of the nucleus from a hot spot at $r \sim 4''$ and from a diffuse radio lobe spreading out from $r \sim 4''$ to $r \sim 9''$. The SW radio lobe is bent to the W relative to the overall axis of the whole jet-like structure (PA ≃ 30°). This distortion of the jet was interpreted by Wilson & Ulvestad (1982) as the signature of the ram pressure of the rotating interstellar gas of the galaxy on the radio plasma. We also detected emission to the northeast of the nucleus from a radio lobe that exhibits a conical limb-brightened morphology (Fig. 1). The VLA maps at 2 cm of Wilson & Ulvestad (1987) were the first to show this morphology for the northeast radio lobe, which was interpreted as the signature of a bow-shock wave driven into the interstellar material as it is compressed by the radio ejecta. The ALMA maps of García-Burillo et al. (2014)

[3] At larger radii we detected a few isolated spots spread mainly across the SB ring; see Fig. 5.

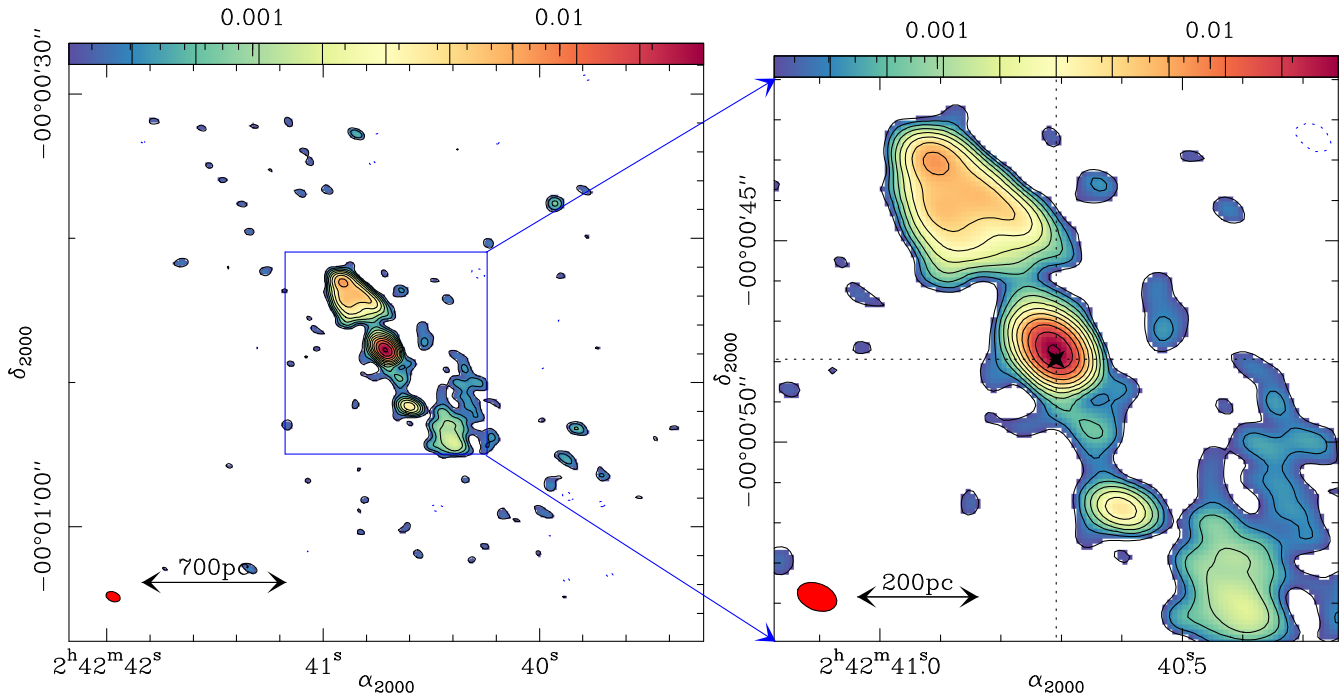

Fig. 1. *Left panel*: continuum emission map of NGC 1068 obtained with ALMA at 86.3 GHz. The map is shown in color scale with contour levels starting at –3σ (dashed contour), and continuing with logarithmic spacing from 3σ to 350σ in steps of 0.21 dex, where 1σ = 80 μJy beam^{-1}. Right panel: same as left panel but zooming in on the inner region. The position of the AGN is highlighted by the star marker. The (red) filled ellipses at the bottom left corners in both panels represent the beam size of ALMA at 86.3 GHz (1.″0 × 0.″7 at PA = 69°).

showed an arc of gas and dust emission located at the edges of the northeast radio lobe. This gas feature, referred to as the bow-shock arc, has anomalous outward velocities interpreted as the result of the expansion of an AGN-driven molecular outflow inside the disk of the galaxy (García-Burillo et al. 2014).

3.2. C_2H map

Figure 2 shows the C_2H(1–0) velocity-integrated intensity map obtained with ALMA in the disk of NGC 1068. We integrated the intensities at each pixel inside the velocity interval defined by $v - v_{\rm sys}^{\rm HEL} \subset [-510, 200]$ km s^{-1}. This window encompasses any potential emission stemming from the four strongest hyperfine components of C_2H(1–0), which are expected to arise at $v - v_{\rm sys}^{\rm HEL} \simeq 0$, –40, –290, and –310 km s^{-1}. When defining the velocity window we further assumed that the disk rotation of NGC 1068 can cause a maximum velocity shift of the line of $\simeq \pm$ 200 km s^{-1} around $v_{\rm sys}^{\rm HEL}$ (Schinnerer et al. 2000; Krips et al. 2011; García-Burillo et al. 2010, 2014).

Figure 3 shows the C_2H(1–0) spectra extracted from a representative set of positions that correspond to strong (>7σ in velocity-integrated units) emission knots in the outflow (OUT-I to OUT-III) and the SB region (SB-I to SB-III). Because of the expected non-negligible velocity gradient inside the ALMA beam caused by rotation, non-circular motions, and turbulence, the individual hyperfine components of the fine groups are blended in all the spectra shown in Fig. 3. We nevertheless resolved in the line profiles the emission from the two fine structure groups, which are shifted to each other by $\simeq$300 km s^{-1}. Hereafter we define the main and secondary group of lines as the two strongest pairs of hyperfine lines that appear blended around $\langle v - v_{\rm sys}\rangle^{\rm HEL} \simeq$ –20 in group-I, and –300 km s^{-1} ($\pm$200 km s^{-1}) in group-II, respectively (see Table 1). No significant emission was detected from the two weakest hyperfine components of C_2H in the individual spectra, i.e., outside the range defined by the main and secondary groups. Emission from these satellite lines should lie at $v - v_{\rm sys}^{\rm HEL} \simeq +110$ and –450 km s^{-1} ($\pm$200 km s^{-1}) and likely have intensities a factor of ~10 lower than the strongest line of the C_2H multiplet, unless the lines were mostly optically thick, which is a scenario that we discard in Sect. 3.3. Therefore we conclude that the interval defined above to derive the velocity-integrated intensities of the C_2H group of lines is not missing any significant emission.

As shown by Fig. 2, a sizeable fraction ($\simeq$65%) of the total (spatially integrated) C_2H line flux recovered by ALMA stems from the SB ring region. Figure 4 shows the overlay of the Paα HST map on the C_2H ALMA map. The SB ring concentrates the bulk of the recent massive star formation in the disk traced by the Paα emission complexes associated with HII regions. The emission of C_2H is mostly prominent at the southwestern end of the SB ring, which is a region hosting an intense star formation activity characterized by strong Paα emission. The molecular line emission in the SB ring is very clumpy and it comes from cloud complexes of $\geq$100 pc-size.

However, the brightest C_2H emission originates from the CND. The morphology of the CND displayed by other molecular tracers imaged by ALMA (García-Burillo et al. 2014; Takano et al. 2014; Tosaki et al. 2017) is to a large extent echoed by C_2H: the CND appears as an elongated ring with two spatially resolved knots of emission asymmetrically located east and west of the AGN locus (denoted as knots OUT-I and OUT-II, respectively; see Fig. 2). The east and west knots are bridged by fainter emission north of the AGN. We also detected significant emission that connects the CND with the outer disk: in the bow-shock arc region (including knot OUT-III; see Fig. 2) to the northeast, and in two emission lanes east and south of the CND.

Figures 4 and 5 show in color contours the Paα and continuum emission, respectively (same as in Fig. 1), on the C_2H

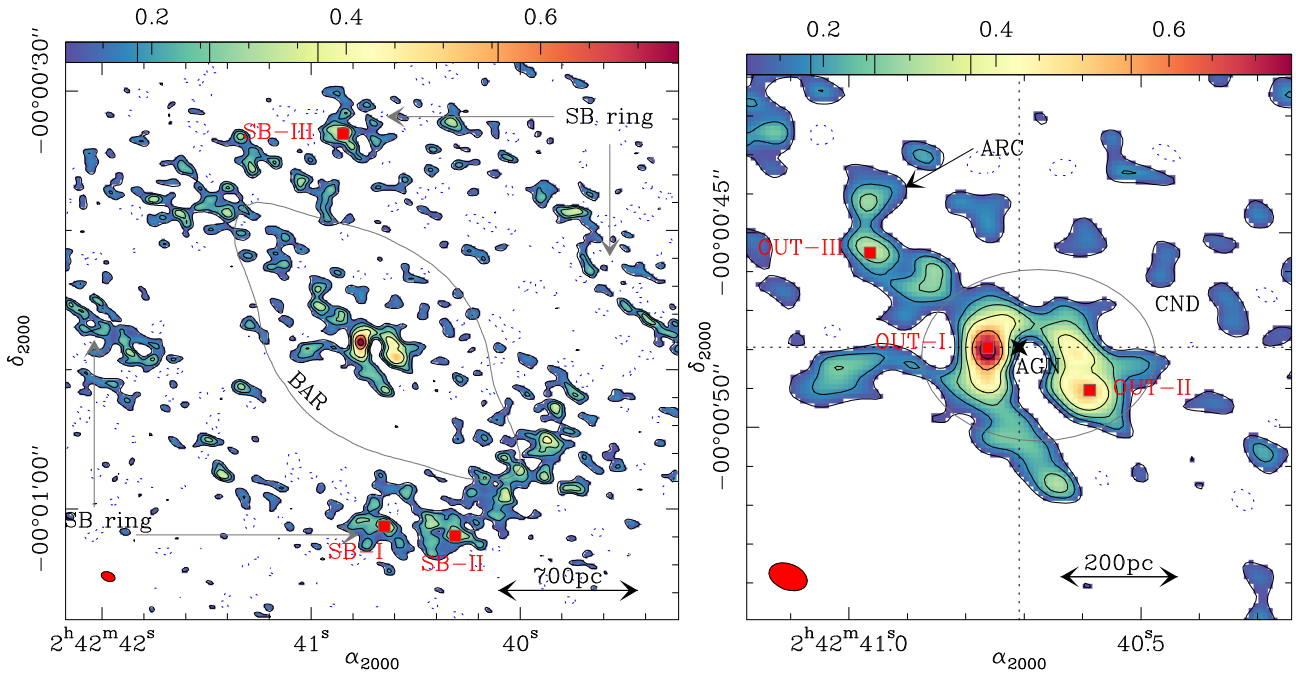

Fig. 2. *Left panel*: $C_2H(1–0)$ integrated intensity map obtained with ALMA in the disk of NGC 1068. The map is shown in color scale with contour levels -3σ (dashed contour), 3σ, 5σ, 7σ, 10σ, 15σ, and 20σ, where $1\sigma = 0.037$ Jy km s^{-1} beam^{-1}. We identify the location of the SB ring and the bar. The latter is identified by a representative isophote of the NIR K-band image of 2MASS (Skrutskie et al. 2006). The (red) square markers highlight the positions of the knots SB-I, SB-II, and SB-III along the SB ring. *Right panel*: same as left panel but zooming in on the outflow region, which extends out to $r \simeq 6''$ (400 pc), as described by García-Burillo et al. (2014). The outflow region comprises the CND and the bow-shock arc. The position of the AGN ($\alpha_{2000} = 02^h42^m40.71^s$, $\delta_{2000} = -00°00'47.94''$) is highlighted by the star marker. The (red) square markers highlight the positions of the knots OUT-I, OUT-II, and OUT-III. The (red) filled ellipses at the bottom left corners in both panels represent the C_2H beam size ($1\farcs0 \times 0\farcs7$ at PA = 69°).

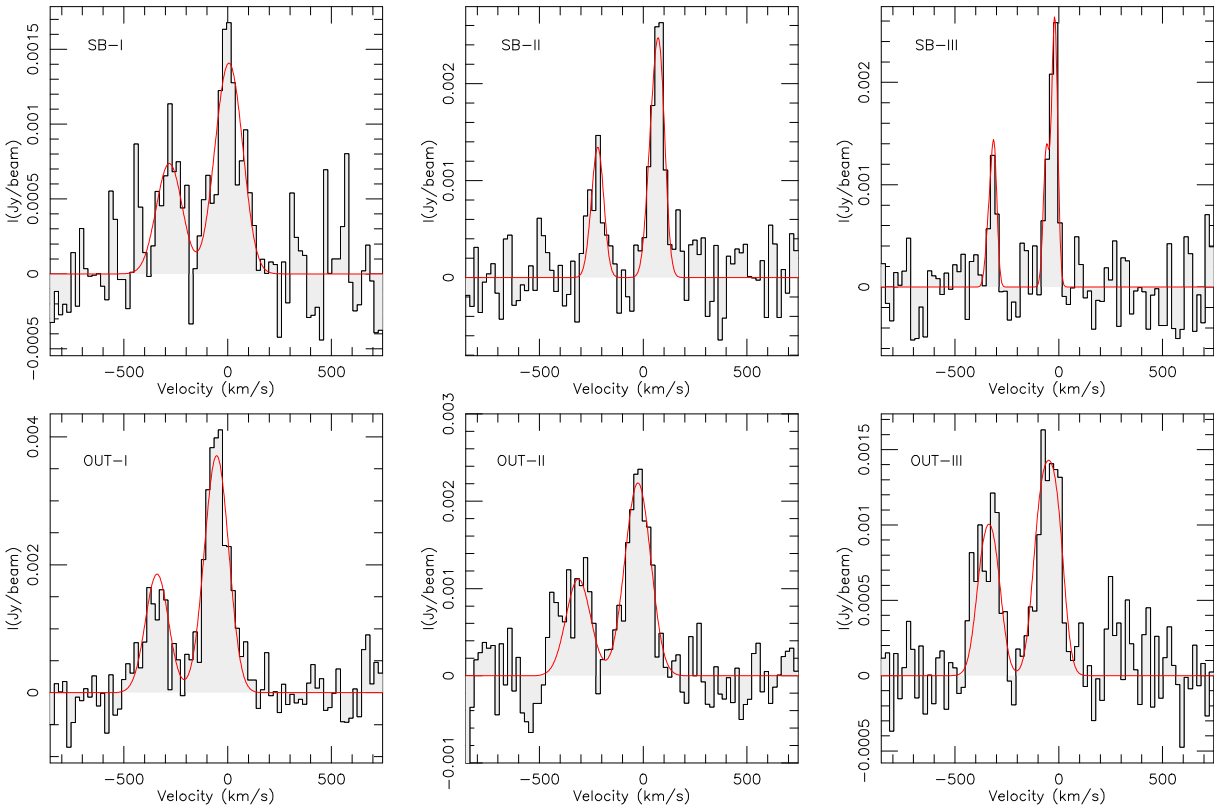

Fig. 3. *Upper panels*: C_2H emission spectra taken at three representative knots of the SB ring (SB-I, SB-II, and SB-III). *Lower panels*: C_2H spectra taken at three representative knots of the outflow region (OUT-I, OUT-II, and OUT-III). The apertures used to extract the spectra correspond to the beam size at the location of each knot ($1\farcs0 \times 0\farcs7$ at PA = 69°). The positions of the knots are defined in Fig. 2. The velocity scale for each spectrum has been derived for the strongest C_2H line at 87.317 GHz (rest frequency) and is relative to $v_{sys}^{HEL} = 1136$ km s^{-1}. The (red) curves show the composite Gaussian profiles of the best fit to the emission, as described is Sect. 3.3.

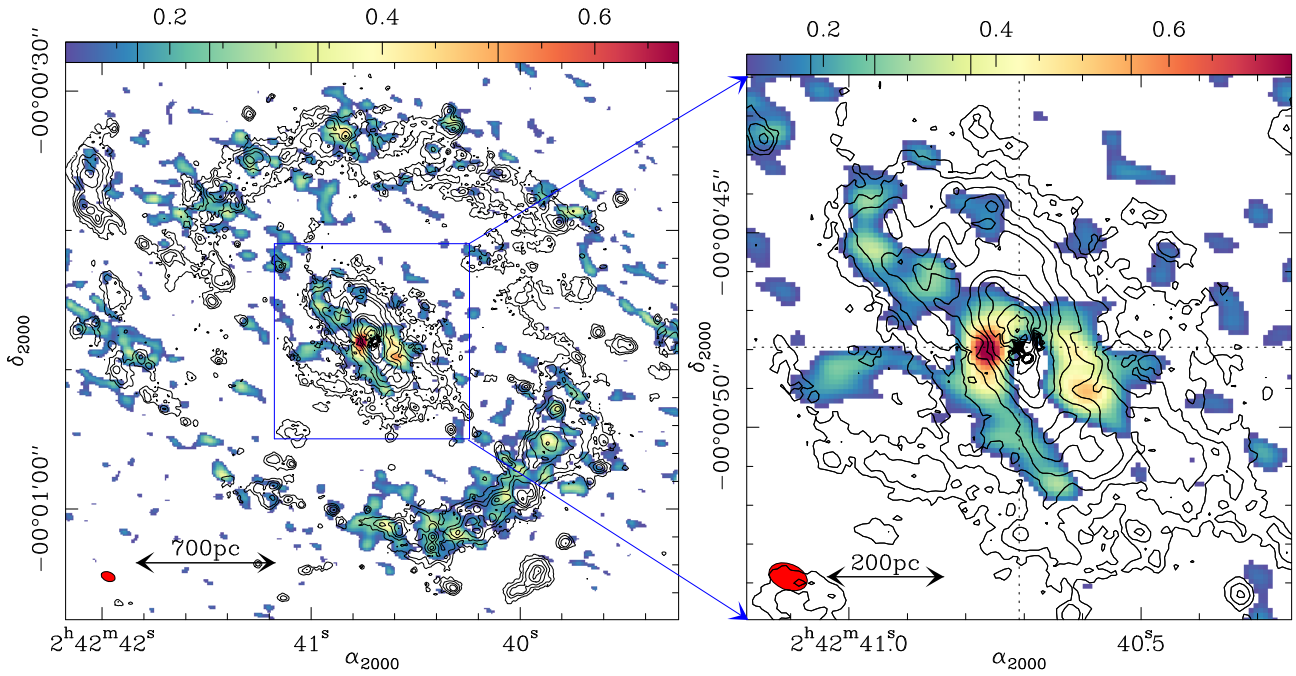

Fig. 4. *Left panel*: overlay of the Paα emission HST map (contours) on the C_2H(1–0) integrated intensity map (color scale as in Fig. 2). Contours of Paα emission are shown with logarithmic spacing from 2.4 to 1600 counts s^{-1} $pixel^{-1}$ in steps of 0.28 dex. *Right panel*: same as left panel but zooming in on the outflow region. The position of the AGN is highlighted by the star marker. The (red) filled ellipses at the bottom left corners in both panels represent the C_2H beam size.

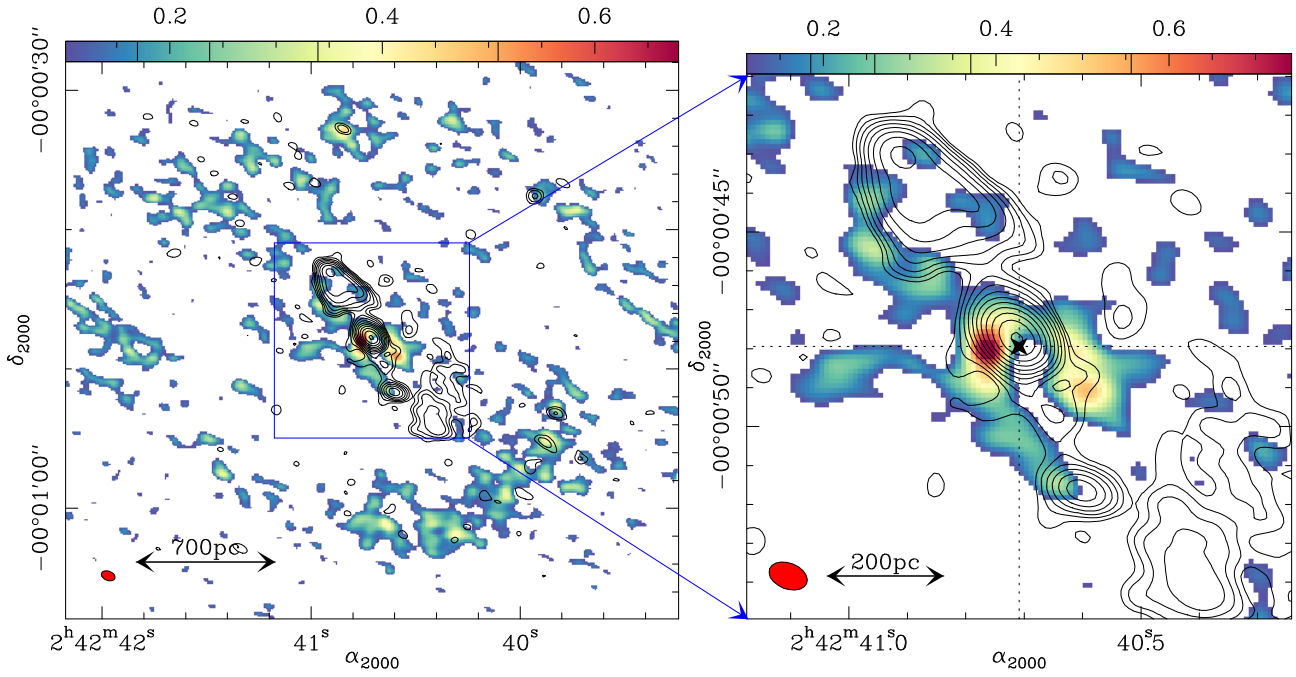

Fig. 5. *Left panel*: overlay of the continuum emission map of NGC 1068 obtained with ALMA at 86.3 GHz (contours) on the C_2H(1–0) integrated intensity map (color scale as in Fig. 2). Contours of continuum emission are shown with logarithmic spacing from 3σ to 350σ in steps of 0.21 dex, where $1\sigma = 80$ μJy $beam^{-1}$. *Right panel*: same as left panel but zooming in on the outflow region. The position of the AGN is highlighted by the star marker. The (red) filled ellipses at the bottom left corners in both panels represent the C_2H beam size.

ALMA map. Figures 4 and 5 offer evidence that the C_2H emission lies at the edges of the AGN ionized nebulosity traced by Paα and radio continuum emission. García-Burillo et al. (2014) analyzed the morphology and kinematics of molecular gas in this region, traced by the CO(3–2) line, and concluded that the NLR gas within the ionization cone is sweeping the ISM of the disk creating a coplanar molecular outflow out to a radius of 400 pc, i.e., a region that comprises the CND and the bow-shock arc feature. The C_2H line seems to probe better than CO the interface between the molecular disk and the ionized gas outflow on the same spatial scales. Hereafter we thus refer to the region encompassing the CND and the bow-shock arc as the outflow region.

Figures 6a and b compare the morphology and kinematics, respectively, of molecular gas in the outflow region derived from the C_2H(1–0) and CO(3–2) images obtained by ALMA.

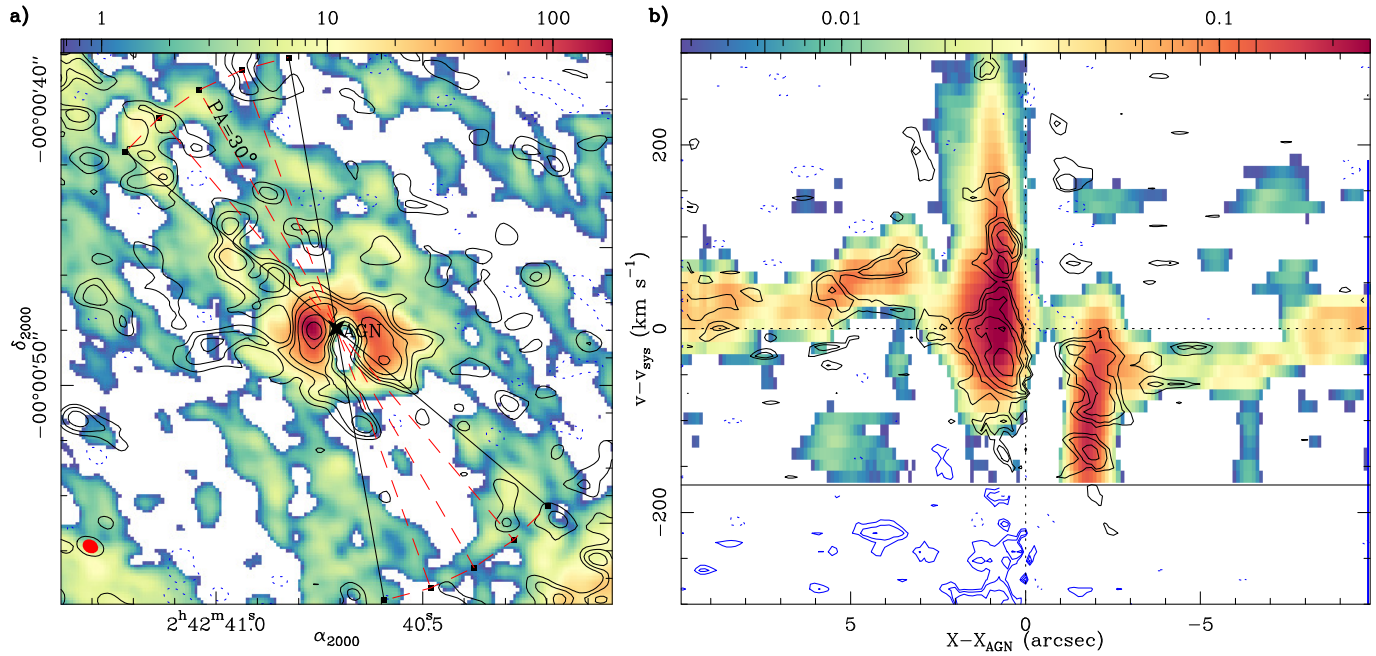

Fig. 6. *Panel a*: overlay of the $C_2H(1–0)$ integrated intensity map (with contours as in Fig. 2) on the CO(3–2) integrated intensity map (with color scale expanding the range [3σ, 800σ], with 1σ = 0.22 Jy km s^{-1}) of García-Burillo et al. (2014) in the central r = 10″ (700 pc) of NGC 1068. The (black) empty and (red) filled ellipses at the bottom left corner represent the C_2H and CO beam sizes, respectively. *Panel b*: comparison of the average position-velocity ($p-v$) plot obtained for the outflow region in $C_2H(1–0)$ (black contours: -2.5σ (dashed contour), 2.5σ, 3.5σ, 5σ, to 9σ by 2σ, with 1σ = 0.18 mJy) and CO(3–2) (color scale: [2σ, 200σ], with 1σ = 1.3 mJy). The averaging has been done using the axes oriented along PA = 10°, 20°, 30°, 40°, and 50° (shown in *a*). The average outflow axis lies at PA = 30°. Blue contours represent the emission stemming from the secondary fine group of the $C_2H(1–0)$ multiplet (group-II). Offsets along the x-axis are measured in arc seconds relative to the AGN locus. Velocity scale is measured for the strongest C_2H line at 87.317 GHz (rest frequency) and is relative to $v_{\rm sys}^{\rm HEL}$ = 1136 km s^{-1}. The black horizontal line indicates the edges of the CO(3–2) band.

The distribution of C_2H shows a good correspondence with the brightest emission clumps of CO in the outflow, both in the CND and bow-shock arc, although the emission of CO is comparatively more widespread than that of C_2H in this region (see Fig. 6a). Figure 6b compares the emission of C_2H and CO in the outflow using the position-velocity ($p-v$) parameter space. With the objective of increasing the signal-to-noise ratio, which is more critical for C_2H, the outflow $p-v$ plot diagrams shown in Fig. 6b were derived by averaging the emission along the five axes shown in Fig. 6a, defined by PA = 10°, 20°, 30°, 40°, and 50°. These axes cover a sizeable fraction of the emission along the molecular outflow, which is oriented along PA = 30° (García-Burillo et al. 2014). Furthermore, with the aim of isolating the non-circular motions associated with the outflow, we subtracted the rotation curve model of García-Burillo et al. (2014) projected along each individual $p-v$ plot before averaging. As illustrated by Fig. 6b, the emission of C_2H closely follows the velocities associated with the CO outflow in this region. A significant fraction of the emission of both molecular tracers lies outside the expected range of virial motions attributable to rotation and dispersion: emission is up to ≥50−200 km s^{-1} redshifted (blueshifted) on the northern (southern) side of the outflow out to $r \simeq 6''$ (400 pc). This reflects the sign and the right order of magnitude of the mean-velocity field deviations seen in the CO(3–2) map of García-Burillo et al. (2014).

3.3. C_2H line opacities

We performed a fit of the spectra shown in Fig. 3 using a comb of four Gaussian profiles that correspond to the strongest hyperfine components of the $C_2H(1–0)$ multiplet. Among the parameters to fit we assumed common widths and excitation temperatures, while optical depth ratios are based on the theoretical line strengths (Tucker et al. 1974). The velocity centroids and optical depths of the strongest component ($\tau_{\rm str}$) were taken as free parameters. Table 2 lists the results obtained in the fit of the spectra shown in Fig. 3. The fit provides the line parameters for the strongest line (J = 3/2−1/2, F = 2−1). We also derived the average secondary-to-main velocity-integrated intensity ratios (R) for the CND, the bow-shock arc, and the SB ring. The optical depths derived from the fits of the two spectra located in the CND (OUT-I and OUT-II) are low, i.e., $\tau_{\rm str} \leq 0.1$ (±0.05). This is in agreement with the average R ratio derived for the CND, $\langle R \rangle \simeq 0.49 \pm 0.05$, which is very close to the optically thin limit for R (≃0.46). The optical depth derived for the knot OUT-III is nevertheless higher $\tau_{\rm str} \simeq 1.3$ (±0.6); this result is in line with the higher average R ratio measured in the bow-shock arc, i.e., $\langle R \rangle \simeq 0.70 \pm 0.09$. The optical depths derived for the SB knots (SB-I, SB-II, and SB-III) are low, i.e., $\tau_{\rm str} \leq 0.1 - 0.2$ (±0.1). The corresponding average R ratio over the SB ring is also low $\langle R \rangle \simeq 0.56 \pm 0.06$.

We can therefore conclude that the lines of the $C_2H(1–0)$ multiplet are mostly optically thin throughout the disk of NGC 1068 with the exception of the bow-shock arc region where opacities may be close to unity[4].

[4] In this scenario of low opacities the intensities of the weakest satellite lines would be at most at a level ≤2σ at the position of the strongest emission knot OUT-I.

Table 2. Parameters of C_2H line fitting results.

KNOT	α_{2000} h m s	δ_{2000} ° ′ ″	$\eta_f \times (T_{ex} - T_{bg}) \times \tau_{str}$ (K)	$(v - v_{sys})_{str}$ (km s^{-1})	$FHWM_{str}$ (km s^{-1})	τ_{str} –
SB-I	02^h:42^m:40.65^s	−00°01′01.2″	$(2.8 \pm 1.0) \times 10^{-1}$	19 ± 8	139 ± 22	0.2 ± 0.6
SB-II	02^h:42^m:40.31^s	−00°01′01.9″	$(5.3 \pm 0.7) \times 10^{-1}$	79 ± 3	63 ± 11	0.1 ± 0.2
SB-III	02^h:42^m:40.85^s	−00°00′33.1″	$(6.6 \pm 0.5) \times 10^{-1}$	-20 ± 2	34 ± 10	0.1 ± 0.3
OUT-I	02^h:42^m:40.76^s	−00°00′48.0″	$(6.8 \pm 0.3) \times 10^{-1}$	-41 ± 3	126 ± 10	0.1 ± 0.1
OUT-II	02^h:42^m:40.59^s	−00°00′49.0″	$(4.1 \pm 1.1) \times 10^{-1}$	-13 ± 5	135 ± 16	0.1 ± 1.9
OUT-III	02^h:42^m:40.96^s	−00°00′45.5″	$(5.4 \pm 1.6) \times 10^{-1}$	-37 ± 5	101 ± 12	1.3 ± 0.7

Notes. All the line parameters correspond to the strongest $C_2H(1-0)$ line ($J = 3/2-1/2$, $F = 2-1$) and are derived according to the procedure described in Sect. 3.3 as follows: T_{ex} is the excitation temperature, T_{bg} is the background temperature (≃2.73 K), η_f is the unknown filling factor of the emission, $(v - v_{sys})_{str}$ is the velocity centroid of the line relative to $v_{sys}^{HEL} = 1136$ km s^{-1}, $FHWM_{str}$ is the half width at half maximum of the line, and τ_{str} is the estimated peak opacity.

3.4. C_2H abundances

In this section we estimate the abundances of C_2H relative to H_2, defined as $X(C_2H) \equiv N(C_2H)/N(H_2)$, both in the SB ring and in the outflow region of NGC 1068.

To estimate the total column densities of C_2H, $N(C_2H)$, we assumed local thermodynamic equilibrium (LTE) conditions for the sake of simplicity. Under the assumption of LTE conditions, the C_2H column densities can be obtained straightforwardly from the intensities of the line. As the velocity-integrated intensities of the C_2H multiplet derived in Sect. 3.2 are a blend of four lines, we first re-normalized the observed intensities by a factor ≃0.46 defined by the expected ratio of intensities of the strongest main line ($J = 3/2-1/2$, $F = 2-1$) to the whole multiplet in the optically thin limit[5]. The validity of the hypothesis of low optical depths for C_2H, which is central to the significance of the LTE estimates, has been discussed in Sect. 3.3. We also needed to assume a value for the excitation temperatures (T_{ex}) for the C_2H emitting gas. As we only have one line multiplet of C_2H, we assumed a range of temperatures (T_{ex} = 10–150 K) that encompasses the total span of kinetic temperatures found by Viti et al. (2014) in their large velocity gradient (LVG) fit of the multiline observations obtained for CO, HCN, and HCO^+ in the different environments of NGC 1068.

In LTE at temperature T_{ex} the column density of the upper level u of a particular transition is related to the total column density of the species via the Boltzmann equation,

$$N = \frac{N_u Z}{g_u e^{-E_u/kT_{ex}}}, \quad (1)$$

where N is the total column density of the species, Z is the partition function evaluated for T_{ex}, g_u is the statistical weight of the level u, and E_u is its energy above the ground state. If the emission is assumed to be optically thin, and if we adopt a filling factor of unity, the column density N_u is related to the observed line intensity,

$$N_u = \frac{8\pi k \nu^2 I}{hc^3 A_{ul}}, \quad (2)$$

where I is the velocity-integrated line intensity (in K km s^{-1}) and A_{ul} is the Einstein coefficient that corresponds to a particular transition, which in our case corresponds to the $J = 3/2 - 1/2$, $F = 2-1$ line of C_2H.

[5] In this scenario the factor is derived from the ratio ≃1/(1 + 0.5 + 0.5 + 0.2) ≃ 0.46.

Table 3. Fractional abundances of C_2H in the SB ring and the outflow regions.

	SB ring	Outflow
T_{ex} = 10 K	$(1.3 \pm 0.7) \times 10^{-8}$	$(1.6 \pm 0.8) \times 10^{-8}$
T_{ex} = 25 K	$(9.7 \pm 4.0) \times 10^{-8}$	$(1.1 \pm 0.4) \times 10^{-7}$
T_{ex} = 50 K	$(4.3 \pm 2.0) \times 10^{-7}$	$(4.8 \pm 2.0) \times 10^{-7}$
T_{ex} = 100 K	$(1.8 \pm 0.8) \times 10^{-6}$	$(2.0 \pm 0.8) \times 10^{-6}$
T_{ex} = 150 K	$(4.2 \pm 2.0) \times 10^{-6}$	$(4.7 \pm 2.0) \times 10^{-6}$

Notes. Abundances are estimated from the C_2H-(1–0) line with gas column densities derived from the dust continuum emission at 349 GHz. We assume LTE conditions and a range of excitation temperatures as explained in Sect. 3.4.

Furthermore, we estimated $N(H_2)$ from the ALMA dust continuum emission map of the galaxy obtained at 349 GHz by García-Burillo et al. (2014) to derive $X(C_2H)$. These observations well probe the molecular gas column densities for the regions studied here: first, because the dust continuum emission at 349 GHz is mostly optically thin, and, second, because the contribution from atomic hydrogen to the total neutral gas content is negligible in the central $r \simeq 30'' \simeq 2$ kpc of the disk (Brinks et al. 1997; García-Burillo et al. 2014). We used a modified blackbody law to derive the dust mass (M_{dust}). In this approach, the fluxes measured in a given aperture, $S_{349\ GHz}$, can be expressed as $S_{349\ GHz} = M_{dust} \times \kappa_{349\ GHz} \times B_{349\ GHz}(T_{dust})/D^2$, where the emissivity of dust at 349 GHz, $\kappa_{349\ GHz} \simeq \kappa_{352\ GHz} \simeq 0.09$ m^2 kg^{-1} (Klaas et al. 2001), $B_\nu(T_{dust})$ is the Planck function, and D is the distance.

The value of M_{dust} per beam was used to predict the associated molecular gas column density map. To this aim, we applied the linear dust/gas scaling ratio of Draine et al. (2007) to the gas-phase oxygen abundances measured in the central 2 kpc of NGC 1068 (∼12 + log(O/H) ∼ 8.8; Pilyugin et al. 2004, 2007), which yields a gas-to-dust mass ratio of $\sim 60^{+30}_{-30}$ (see discussion in García-Burillo et al. 2014). Finally, we degraded the spatial resolution of the resulting column density map to match that of the C_2H map prior to obtaining a map for $X(C_2H)$.

Table 3 lists the mean fractional abundances of C_2H as estimated by our LTE analysis for the reported range of T_{ex}. In the interest of exploring any potential difference between the SB and outflow, we spatially averaged $X(C_2H)$ inside these two regions, as defined in Sect. 3.2. As expected, the values of $X(C_2H)$ depend heavily on the assumed T_{ex}. For a given T_{ex}, the abundance of C_2H is marginally ≃10–20% higher in the outflow region than

in the SB ring; with a common lower limit of $X(C_2H) \simeq$ a few 10^{-8}, for the lowest temperature we assumed $T_{ex} = 10$ K. This is close to the formal lower limit on $T_{ex} \geq 8$ K, which is derived from the values fitted for $\eta_f \times (T_{ex} - T_{bg}) \times \tau_{str}$ that are listed in Table 3. This lower limit is formally obtained by assuming a very conservative upper limit on the filling factors $\eta_f \leq 1$. All in all, the reported high abundances of C_2H found in the SB ring and outflow for $T_{ex} = 10$ K are both comparable to those found in Galactic and extragalactic PDRs associated with massive star formation. However, although this scenario seems plausible in the SB ring, where molecular gas is currently feeding a massive star formation episode in NGC 1068, the evidence of a similar level of star formation activity that may sustain these high abundances of C_2H in the molecular outflow is less clear. This suggests that a different mechanism is at play in this region.

For temperatures $T_{ex} \geq 25$ K the derived C_2H abundances lie in the range $X(C_2H) \simeq 10^{-7}-10^{-6}$. These higher temperatures are specifically required to fit the multiline CO dataset of the outflowing CND (Viti et al. 2014). In particular, Viti et al. (2014) used LTE to conclude that the rotational temperature, T_{rot}, of the CO emitting gas in the CND $\simeq$ 40–60 K. This is also in excellent agreement with the values of the dust temperature required to fit the SED of dust emission in the outflow region out to $r \leq 400$ pc, where $T_{dust} \simeq 46 \pm 3$ K (García-Burillo et al. 2014). Furthermore Viti et al. (2014) used non-equilibrium radiative transfer schemes (RADEX) to conclude that the kinetic temperature of molecular gas traced by CO lines in the outflow is significantly high, i.e., ≥100 K. In contrast, a similar analysis suggests that kinetic temperatures of molecular gas are comparatively a factor ≃2–3 lower in the SB ring.

In order to nail down more accurately how $X(C_2H)$ changes in the different environments of NGC 1068, we would need to estimate T_{ex} for C_2H independently by observing at least 1–2 higher N transitions. However, if we assume that the excitation of C_2H follows a pattern similar to the rest of molecular species, the observational evidence discussed above suggests that T_{ex} is likely a factor of 2–3 higher in the outflow region compared to the SB ring, and, also, that ≃10 K is a conservative lower limit for T_{ex} in either case. We therefore adopt the following reference values for $X(C_2H)$: ≃ a few 10^{-8} in the SB ring for $T_{ex} \simeq 10$ K, and ≃ a few 10^{-7} in the outflow region for $T_{ex} \simeq 25-50$ K.

4. Origin of the C_2H abundances

In this section we aim to account for the range of abundances derived in Sect. 3.4 for C_2H in the SB ring and outflow region of NGC 1068 using a set of time-dependent gas-grain chemical models, parametrized shock models, and gas-phase PDR models.

4.1. Chemical models: description

A comprehensive chemical modeling of the C_2H molecule is beyond the scope of this observational paper. Moreover, we are aware of the limitations of having observed only one N transition of the C_2H multiplet, leading to an uncertain derivation of the fractional abundance. Hence we can only qualitatively discuss the origin of this emission and its potential role as a tracer of distinct gas components. We used and augmented the grid of chemical models from Viti (2017) run with the UCL_CHEM time dependent gas-grain chemical model (Viti et al. 2011), which includes a parametrized shock module (Jiménez-Serra et al. 2008) and a very small grid of PDR models taken from Bell et al. (2006) and Vasta et al. (2010), run with the UCL_PDR code. We assumed for all the models a solar C/O abundance ratio ~0.6. Below we briefly present the codes, which are more extensively described in the above references.

The code UCL_CHEM[6] is a time dependent gas-grain chemical model that computes the evolution of chemical abundances of the gas and on the ices as a function of time, starting from a diffuse and atomic gas. The code is coupled with the parametrized shock model of Jiménez-Serra et al. (2008). The code is run in two distinct temporal phases denoted as Phase I and Phase II. The initial density in Phase I is ~10 cm^{-3}. The gas is allowed to collapse and reach a high density by means of a free-fall collapse process. In this context the collapse is not meant to represent the formation of protostars, but it is simply a way to compute the chemistry of high density gas in a self-consistent way starting from a diffuse atomic gas, i.e., without assuming the chemical composition at its final density. The temperature during this phase is kept constant at 10 K and the cosmic-ray ionization rates and radiation fields are at their standard Galactic values ($\zeta_0 = 5 \times 10^{-17}$ s^{-1} and 1 Draine field ≡ 2.74×10^{-3} erg s^{-1} cm^{-2}, respectively). During Phase I atoms and molecules are allowed to freeze onto the dust grains and react with each other, forming icy mantles. Nonthermal desorption is also included. In Phase II, for the non-shock models, UCL_CHEM computes the chemical evolution of the gas and the icy mantles after either an assumed burst of star formation or an AGN activity episode has occurred. The temperature of the gas increases from 10 K to a value set by the user, and thermal sublimation from the icy mantles occurs. The chemical evolution of the gas is then followed for 10^7 yr. In the shock models, Phase II considers a plane-parallel C-shock propagating with a velocity, V_s, through the ambient medium.

One of the effects of the AGN activity on the gas is an enhanced cosmic-ray and/or X-ray ionization rate. The grid of models we employed from Viti (2017) uses the cosmic-ray ionization flux to simulate an enhancement in X-ray flux as well. Although this approximation has its limitations in that the X-ray flux ionizes and heats the gas more efficiently than cosmic rays, the chemistry arising from these two fluxes should be similar and the chemical trends are the same for cosmic rays and X-rays for a fixed gas temperature, which is what is assumed in these models (see also Viti et al. 2014).

While some of the models from the UCL_CHEM grid may be considered as representative of PDR models, since the radiation field is enhanced enough to penetrate great depths and hence affect the chemistry, we also considered a very small grid of pure gas-phase PDR models at lower gas density. The latter would be more representative of the diffuse and translucent clouds where C_2H has been observed at fractional abundances of ~10^{-8} (e.g., Turner et al. 1999) and where the temperature is highly affected by the UV radiation field. These models were run with a self-consistent PDR model: the UCL_PDR code is a 1D time dependent PDR code. It was first developed by Bell et al. (2005, 2006) and further augmented by Bayet et al. (2012) and Priestley et al. (2017). The code assumes a semi-infinite slab geometry and computes the chemistry and temperature as functions of depth and time within the semi-infinite slab. The chemistry and thermal balance are calculated self-consistently at each depth point into the slab and at each time-step, producing chemical abundances, emission line strengths, and gas temperatures as a function of depth and time. The code has been benchmarked (Röllig et al. 2007).

[6] Now publicly available at `https://uclchem.github.io` and published in Holdship et al. (2017).

Table 4. Grid of PDR models (UCL_PDR).

Model	ζ (ζ_0)	χ (Draine field)	n_H (cm^{-3})
48	1.0	10	10^3
49	1.0	100	10^3
50	1.0	1000	10^3
51	10	100	10^3

Notes. Column (1) lists the model number. Columns (2) and (3) list the cosmic-ray ionization rates (ζ) and radiation fields (χ), respectively, in units of their standard Galactic values ($\zeta_0 = 5 \times 10^{-17}$ s^{-1} and 1 Draine field $\equiv 2.74 \times 10^{-3}$ erg s^{-1} cm^{-2}). Column (4) lists the hydrogen gas density (n_H). For the PDR models the temperature varies with depth and is not listed.

4.2. Chemical models: results

Tables 4–6 list, respectively, the parameters of the grid of UCL_PDR, UCL_CHEM, and shock models we considered. We computed all our models with solar abundances.

We note that none of the pure gas-phase low density (10^3 cm^{-3}) PDR models (Models 48−51; Table 4), at any time or depth into the cloud, succeed in achieving a fractional abundance of C_2H larger than 10^{-9}. This is consistent with the results of previous PDR models. For example, Turner et al. (1999) succeeded in fitting the C_2H abundance observed in some translucent clouds (10^{-8}) with steady-state models but only by assuming a high non-solar C/O ratio (~0.9). In denser PDRs Cuadrado et al. (2015) found that a C_2H abundance of 10^{-8} can in fact only be matched by a model with a gas density of $>10^6$ cm^{-3}, radiation field of $>10^4$ Draine field, and at a depth <2 mag. In other words, only an extremely dense but thin layer of gas can steadily sustain such a high abundance of C_2H. Such a scenario is depicted by some of our models from the UCL_CHEM grid and these models are discussed later.

We now discuss the output of Models 1−44 (Table 5) in the light of the abundances derived for the outflow region. If we assume the temperature of the gas is >50 K then none of the UCL_CHEM models at equilibrium succeed in producing enough C_2H, with maximum abundances that reach at most $\simeq 3 \times 10^{-8}$. However, there is a class of models, namely Models 13, 23, 35, where higher abundances, comparable to (or higher than) those observed, can be reached at very early times. These models are all characterized by either a higher (by a factor of 10) than standard UV radiation field, or by a very high cosmic-ray ionization rate (a factor of 5000 higher than standard); the latter would account for the influence of enhanced X-ray irradiation. All models have at least a density of 10^4 cm^{-3}. We plot in Fig. 7 the temporal evolution of C_2H for these models. The increase and decrease of C_2H are due to photodissociation of C_2H_2 and ion-neutral reaction of C_2H with C^+, respectively. While we cannot differentiate between a UV or a X-ray enhanced field, all these models are consistent with those of molecular interfaces between outflows and ambient clouds in high-mass star-forming regions in our Galaxy (Codella et al. 2006; van Kempen et al. 2010; San José-García et al. 2016), where visual extinctions are low (≤2 mag), gas densities, temperatures, and radiation fields are high ($>10^4$ cm^{-3}, >100 K, and >10 Draine field, respectively), and the gas is short-lived ($\simeq 10^{2-3}$ yr). We find that these transient conditions in the UV or X-ray irradiated gas may be due to non-dissociative shocks associated with the highly turbulent interface between the outflow and molecular clouds. While it is true that Model 23 has a high visual extinction, because of the very high cosmic-ray ionization rate the chemistry of the gas is effectively the same as that of an interface. Although timescales

Table 5. Grid of gas-grain chemical models (UCL_CHEM).

Model	ζ (ζ_0)	χ (Draine field)	T_k (K)	n_H (cm^{-3})	A_V (mag)
1	1.0	1.0	100.0	10^4	1
2	1.0	1.0	100.0	10^4	50
3	1.0	1.0	100.0	10^5	1
4	1.0	1.0	100.0	10^5	50
5	1.0	1.0	100.0	10^6	50
6	10.0	1.0	100.0	10^4	1
7	10.0	1.0	100.0	10^4	50
8	10.0	1.0	100.0	10^5	1
9	10.0	1.0	100.0	10^5	50
10	10.0	1.0	100.0	10^6	50
11	1.0	10.0	100.0	10^4	1
12	1.0	10.0	100.0	10^4	50
13	1.0	10.0	100.0	10^5	1
14	1.0	10.0	100.0	10^5	50
15	1.0	10.0	100.0	10^6	50
16	10.0	10.0	100.0	10^4	1
17	10.0	10.0	100.0	10^4	50
18	1.0	500.0	100.0	10^4	1
19	1.0	500.0	100.0	10^4	50
20	500.0	1.0	100.0	10^4	1
21	500.0	1.0	100.0	10^4	50
22	5000.0	1.0	100.0	10^4	1
23	5000.0	1.0	100.0	10^4	10
24	0.0	1.0	100.0	10^5	1
25	0.0	1.0	100.0	10^5	50
26	1.0	1.0	200.0	10^5	1
27	1.0	1.0	200.0	10^5	50
28	1.0	1.0	200.0	10^4	1
29	1.0	1.0	200.0	10^4	50
30	1.0	1.0	200.0	10^6	50
31	10.0	1.0	200.0	10^6	50
32	1.0	10.0	200.0	10^6	50
33	10.0	1.0	200.0	10^5	1
34	10.0	1.0	200.0	10^5	50
35	1.0	10.0	200.0	10^5	1
36	1.0	10.0	200.0	10^5	50
37	1.0	1.0	50.0	10^4	1
38	1.0	1.0	50.0	10^4	50
39	1.0	1.0	50.0	10^5	50
40	1.0	1.0	50.0	10^6	50
41	1.0	1.0	100.0	10^6	2
42	1.0	100.0	100.0	10^6	2
43	1.0	10^3	100.0	10^6	2
44	1.0	10^4	100.0	10^6	2

Notes. Column (1) lists the model number. Columns (2) and (3) list the cosmic-ray ionization rates (ζ) and radiation fields (χ), respectively, in units of their standard Galactic values ($\zeta_0 = 5 \times 10^{-17}$ s^{-1} and 1 Draine field $\equiv 2.74 \times 10^{-3}$ erg s^{-1} cm^{-2}). Columns (4) and (5) list the kinetic temperature (T_k) and hydrogen density (n_H), respectively, of the gas. Column (6) lists the depth of the layer in A_V-units.

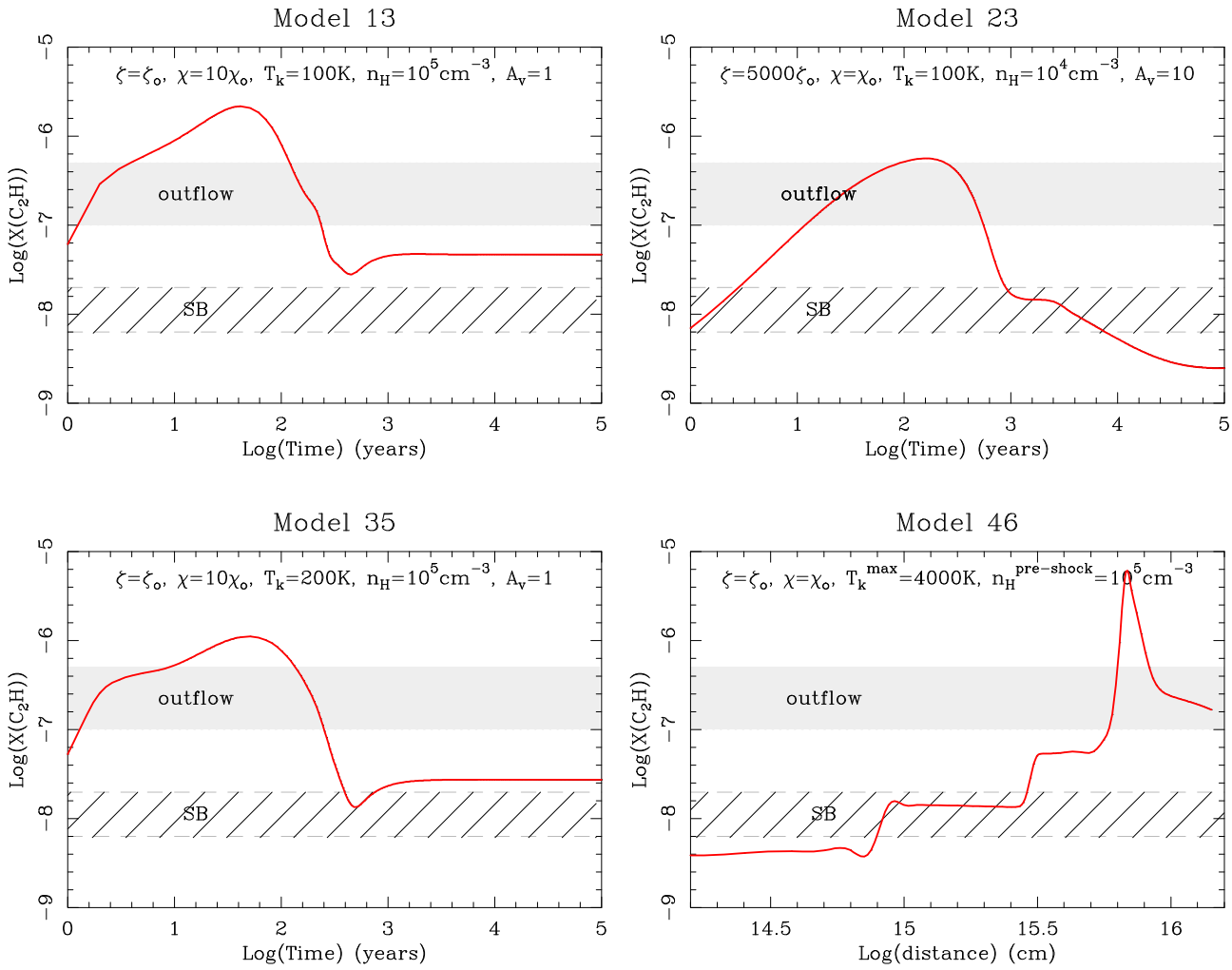

Fig. 7. Fractional abundance of C_2H for a representative set of chemical models discussed in Sect. 4 that account for the measured abundances of ethynyl in the SB ring and the outflow region of NGC 1068. The C_2H abundance is represented as a function of time for gas-grain chemical models (UCL_CHEM) number 13, 23, and 35, and as a function of distance for shock model number 46. This scale corresponds to the distance that the shock travels up to the dissipation length, which is the length scale over which the shock dissipates, beyond which the model is no longer applicable (see Jiménez-Serra et al. 2008). The main parameters of the models, extensively described in Sect. 4 and listed in Tables 4–6, are indicated in each panel. We highlight the range of C_2H abundances measured in the SB ring ($\simeq$ a few 10^{-8} for $T_{ex} \simeq 10$ K) and in the outflow region ($\simeq$ a few 10^{-7} for $T_{ex} \simeq 25$–50 K).

Table 6. Grid of parametrized shock models.

Model	ζ (ζ_0)	χ (Draine field)	T_{max} (K)	$n_{H_{pre\text{-}shock}}$ (cm^{-3})
45	1.0	1.0	2200	10^4
46	1.0	1.0	4000	10^5
47	1.0	1.0	4000	10^6

Notes. Column (1) lists the model number. Columns (2) and (3) list the cosmic-ray ionization rates (ζ) and radiation fields (χ), respectively, in units of their standard Galactic values ($\zeta_0 = 5 \times 10^{-17}$ s^{-1} and 1 Draine field $\equiv 2.74 \times 10^{-3}$ erg s^{-1} cm^{-2}). Columns (4) and (5) list the maximum kinetic temperature (T_{max}) and pre-shock hydrogen density ($n_{H_{pre\text{-}shock}}$) of the gas, respectively.

may be very short, the continual erosion of dense material by the wind or outflow would resupply the interface, so a nearly steady state may persist in the UV or X-ray illuminated gas across the shock front.

Models 1–44, although partly mimicking the effects of nondissociative shocks, did not properly model the passage of the shock. In order to test our hypothesis that the C_2H abundances can be reproduced by the erosion of icy mantles due to the passage of nondissociative shocks, we also included in our grid three shock models (45–47; Table 6). In these models we assumed an average shock velocity $V_s \simeq 40$ km s^{-1}. The preshock density and the shock velocity determine the maximum temperature reached (see Table 6). We plot the results of Model 46 in Fig. 7. It is clear that the C_2H abundance does indeed rise as the shock penetrates the dissipation length of the gas, and it is close to that found by our LTE analysis if one assumes a 100 K gas, which, especially in the outflow region, is a reasonable gas temperature (García-Burillo et al. 2014; Viti et al. 2014).

With all the necessary caveats in mind, these results suggest that the inferred high abundances of C_2H in the outflow could represent the first evidence of a chemical fingerprint of an outflow interface region in an external galaxy. The scenario described above, where UV or X-ray radiation and shocks seem to act in concert to shape the chemistry of the outflow interface

region in NGC 1068, is also similar to that supporting the existence of mechanical dominated regions (MDRs), which is a variant of PDRs in which mechanical action is invoked to explain the spectral energy distribution of CO in some star-forming and active galaxies (Meijerink et al. 2013; Rosenberg et al. 2014, 2015).

We now examine the results of Models 1–44 in the light of the abundances derived for the SB ring. While the derived fractional abundances as a function of temperatures are essentially the same as in the outflow spot, the derived temperatures are comparatively lower in the SB ring (Sect. 3.4) and since C_2H may be subthermally excited, the derived fractional abundances may nevertheless correspond to those derived for a gas at a higher (than 10 K) excitation temperature. In this case, the abundances that our models need to match are more of the canonical order of $\sim 10^{-8}$. We first look at the models run with a temperature of 50 K (Models 37–40). In fact Model 37, which represents a canonical PDR, with Galactic UV and cosmic-ray ionization fields, a typical molecular cloud gas density of 10^4 cm^{-3}, visual extinction of 1 mag, and temperature of 50 K provides us with a match with an abundance of 10^{-8}. This may therefore indicate that C_2H is simply tracing the gas most exposed to star formation in a region where we know star formation is very active. Other models match this abundance at equilibrium as well: in particular Models 1, 11, 13, and 16, all at $A_V = 1$ mag (hence PDR-like), and differing by a factor of 10 in either radiation field, cosmic-ray ionization field and gas density from Model 37, hence all reasonable PDR models depicting gas affected by active star formation, as expected in a SB ring. However, all these models are run at gas temperatures of 100 K. Moreover, Models 41–44 mimick the best-fit models from Cuadrado et al. (2015) and, of those, Models 42–44 are able to reproduce the observed abundance of $1-3\times10^{-8}$, making it difficult to determine whether C_2H is tracing a very dense gas subjected to an enhanced radiation field or a more canonical molecular cloud gas. Regardless, the C_2H must come from a very low visual extinction gas, which means that the SB ring must be at least partly dominated by PDR gas. Hence for the SB ring, C_2H may simply be tracing star formation activity.

Further confirmation of all the favored scenarios discussed above would need a more extensive chemical modeling that explores, for example, a wider range of initial conditions, including initial elemental abundances differing from solar.

5. Summary and conclusions

We used ALMA to map the emission of the hyperfine multiplet of $C_2H(1-0)$ and its underlying continuum emission at 86.3 GHz in the central $r \simeq 35''$ (2.5 kpc) region of the disk of the nearby (D = 14 Mpc) Seyfert 2 galaxy NGC 1068 with a spatial resolution $1\farcs0 \times 0\farcs7$ (≃50–70 pc). In an attempt to explain the fractional abundances derived for C_2H in the different spatially resolved environments of the galaxy we developed a set of time-dependent chemical models.

We summarize the main results of our study as follows:

- We detected widespread C_2H emission in the disk of NGC 1068. Most (≃65%) of the spatially integrated C_2H line flux stems from the $r \simeq 1.3$ kpc SB molecular ring. The SB ring concentrates the bulk of the recent massive star formation in the disk of the galaxy as traced by the strong Paα emission of HII regions imaged by HST. The brightest C_2H emission originates nevertheless from the $r \simeq 200$ pc outflowing CND. We also detected significant C_2H emission bridging the CND with the outer disk in a region that probes the interface between the molecular disk and the ionized gas outflow out to $r \simeq 400$ pc.
- The line ratios measured between the hyperfine components of the C_2H multiplet detected throughout the disk of NGC 1068 indicate that their emission is mostly optically thin. We derived the column densities of C_2H assuming LTE conditions and a set of excitation temperatures constrained by the previous multiline CO studies of the galaxy.
- Maps of the dust continuum emission obtained at 349 GHz by ALMA were used to calculate the H_2 gas column densities. These were used in combination with the C_2H column densities derived from LTE to obtain the fractional abundances of this species in different regions. Our estimates range from $X(C_2H) \simeq$ a few 10^{-8} in the SB ring up to $X(C_2H) \simeq$ a few 10^{-7} in the outflow.
- We performed a preliminary qualitative chemical analysis to determine the origin of the high abundance of C_2H in the outflow and the SB ring. In both regions we find that the gas is dense ($\geq 10^4$ cm^{-3}), confirming previous results (García-Burillo et al. 2014; Viti et al. 2014).
- In the outflow we found that fractional abundances of $X(C_2H) \simeq$ a few 10^{-7} can only be reached at very early times in models where dense molecular gas is heavily irradiated by UV or X-ray photons. In particular, these models are consistent with those of molecular interfaces between outflows and ambient clouds, where visual extinctions are low (≤2 mag), gas densities, temperatures, and UV fields or cosmic-ray fields are high ($>10^4$ cm^{-3}, >100 K, and >10 Draine field, or >5000 ζ_0, respectively), and the gas is short-lived ($\simeq 10^{2-3}$ yr).
- We found that transient conditions in the outflow may be due to UV or X-ray irradiated nondissociative shocks associated with the highly turbulent interface between the outflow and molecular clouds. Although timescales may be very short, the continual erosion of dense material by the wind or jet resupplies the interface, so a nearly steady state persists (e.g., Codella et al. 2006). Shock models seem to confirm that C_2H can also be enhanced from icy mantle sputtering.
- In the SB ring, on the other hand, an abundance of $X(C_2H) \simeq$ a few 10^{-8} is either tracing molecular gas typical of the skin of Galactic giant molecular clouds or is tracing a much denser skin subjected to an enhanced UV field. Both scenarios are consistent with active star formation.

Our chemical modeling is not extensive and has not covered a large enough parameter space of initial conditions to exclude the validity of alternative scenarios. In particular, we cannot exclude that the hydrocarbons chemistry is incomplete in our models or that PAH chemistry (not included) has a significant effect on the gas-phase chemistry of C_2H (e.g., Pety et al. 2005); equally a small difference in the C/O ratio in the adopted initial abundances of our models could change our conclusions as this would affect the abundance of all hydrocarbons (Cuadrado et al. 2015). Once further transitions of C_2H are obtained, a more comprehensive modeling would be needed to shed light on the origin of the significantly high abundances of C_2H in NGC 1068.

Acknowledgements. We acknowledge the staff of ALMA in Chile and the ARC-people at IRAM-Grenoble in France for their invaluable help during the data reduction process. This paper makes use of the following ALMA data: ADS/JAO.ALMA#2013.1.00055.S and #2011.0.00083.S. ALMA is a partnership of ESO (representing its member states), NSF (USA), and NINS (Japan) together with NRC (Canada) and NSC and ASIAA (Taiwan), in cooperation with the Republic of Chile. The Joint ALMA Observatory is operated by ESO, AUI/NRAO, and NAOJ. The National Radio Astronomy Observatory is a facility

of the National Science Foundation operated under cooperative agreement by Associated Universities, Inc. We used observations made with the NASA/ESA *Hubble* Space Telescope, and obtained from the *Hubble* Legacy Archive, which is a collaboration between the Space Telescope Science Institute (STScI/NASA), the Space Telescope European Coordinating Facility (ST-ECF/ESA), and the Canadian Astronomy Data Centre (CADC/NRC/CSA). S.G.B. and A.U. acknowledge support from the Spanish MINECO and FEDER funding grants AYA2016-76682-C3-2-P, AYA2016-79006-P, and ESP2015-68964-P. C.R.A. acknowledges the Ramón y Cajal Program of the Spanish Ministry of Economy and Competitiveness through project RYC-2014-15779 and the Spanish Plan Nacional de Astronomía y Astrofísica under grant AYA2016-76682-C3-2-P. A.A.H. acknowledges support from the Spanish MINECO and FEDER funding grant AYA2015-6346-C2-1-P.

References

Aladro, R., Martín, S., Martín-Pintado, J., et al. 2011, A&A, 535, A84
Aladro, R., Viti, S., Bayet, E., et al. 2013, A&A, 549, A39
Bayet, E., Viti, S., Hartquist, T. W., & Williams, D. A. 2011a, MNRAS, 417, 627
Bayet, E., Williams, D. A., Hartquist, T. W., & Viti, S. 2011b, MNRAS, 414, 1583
Bayet, E., Davis, T. A., Bell, T. A., & Viti, S. 2012, MNRAS, 424, 2646
Bell, T. A., Viti, S., Williams, D. A., Crawford, I. A., & Price, R. J. 2005, MNRAS, 357, 961
Bell, T. A., Roueff, E., Viti, S., & Williams, D. A. 2006, MNRAS, 371, 1865
Beuther, H., Semenov, D., Henning, T., & Linz, H. 2008, ApJ, 675, L33
Bland-Hawthorn, J., Gallimore, J. F., Tacconi, L. J., et al. 1997, Ap&SS, 248, 9
Brinks, E., Skillman, E. D., Terlevich, R. J., & Terlevich, E. 1997, Ap&SS, 248, 23
Codella, C., Viti, S., Williams, D. A., & Bachiller, R. 2006, ApJ, 644, L41
Costagliola, F., Aalto, S., Rodriguez, M. I., et al. 2011, A&A, 528, A30
Cuadrado, S., Goicoechea, J. R., Pilleri, P., et al. 2015, A&A, 575, A82
Draine, B. T., Dale, D. A., Bendo, G., et al. 2007, ApJ, 663, 866
Endres, C. P., Schlemmer, S., Schilke, P., Stutzki, J., & Müller, H. S. P. 2016, J. Mol. Spectr., 327, 95
Fuente, A., Martin-Pintado, J., Cernicharo, J., & Bachiller, R. 1993, A&A, 276, 473
Gallimore, J. F., Baum, S. A., O'Dea, C. P., & Pedlar, A. 1996, ApJ, 458, 136
Gallimore, J. F., Baum, S. A., & O'Dea, C. P. 2004, ApJ, 613, 794
Gallimore, J. F., Elitzur, M., Maiolino, R., et al. 2016, ApJ, 829, L7
García-Burillo, S., Usero, A., Fuente, A., et al. 2010, A&A, 519, A2
García-Burillo, S., Combes, F., Usero, A., et al. 2014, A&A, 567, A125
García-Burillo, S., Combes, F., Ramos Almeida, C., et al. 2016, ApJ, 823, L12
Hailey-Dunsheath, S., Sturm, E., Fischer, J., et al. 2012, ApJ, 755, 57
Heikkilä, A., Johansson, L. E. B., & Olofsson, H. 1999, A&A, 344, 817
Henkel, C., Schilke, P., & Mauersberger, R. 1988, A&A, 201, L23
Holdship, J., Viti, S., Jiménez-Serra, I., Makrymallis, A., & Priestley, F. 2017, AJ, 154, 38
Huggins, P. J., Carlson, W. J., & Kinney, A. L. 1984, A&A, 133, 347
Imanishi, M., & Nakanishi, K. 2013, AJ, 146, 47
Imanishi, M., Nakanishi, K., & Izumi, T. 2016, ApJ, 822, L10
Israel, F. P. 2009, A&A, 493, 525
Jiménez-Serra, I., Caselli, P., Martín-Pintado, J., & Hartquist, T. W. 2008, A&A, 482, 549
Kamenetzky, J., Glenn, J., Maloney, P. R., et al. 2011, ApJ, 731, 83
Kelly, G., Viti, S., García-Burillo, S., et al. 2017, A&A, 597, A11
Klaas, U., Haas, M., Müller, S. A. H., et al. 2001, A&A, 379, 823
Kohno, K., Matsushita, S., Vila-Vilaró, B., et al. 2001, in The Central Kiloparsec of Starbursts and AGN: The La Palma Connection, eds. J. H. Knapen, J. E. Beckman, I. Shlosman, & T. J. Mahoney, ASP Conf. Ser., 249, 672
Krips, M., Neri, R., García-Burillo, S., et al. 2008, ApJ, 677, 262
Krips, M., Martín, S., Eckart, A., et al. 2011, ApJ, 736, 37
Li, J., Wang, J., Gu, Q., Zhang, Z.-Y., & Zheng, X. 2012, ApJ, 745, 47
Martín, S., Mauersberger, R., Martín-Pintado, J., Henkel, C., & García-Burillo, S. 2006, ApJS, 164, 450
Martín, S., Verdes-Montenegro, L., Aladro, R., et al. 2014, A&A, 563, L6
Martín, S., Kohno, K., Izumi, T., et al. 2015, A&A, 573, A116
Meier, D. S., & Turner, J. L. 2005, ApJ, 618, 259
Meier, D. S., & Turner, J. L. 2012, ApJ, 755, 104
Meier, D. S., Walter, F., Bolatto, A. D., et al. 2015, ApJ, 801, 63
Meijerink, R., Kristensen, L. E., Weiß, A., et al. 2013, ApJ, 762, L16
Nakajima, T., Takano, S., Kohno, K., & Inoue, H. 2011, ApJ, 728, L38
Nakajima, T., Takano, S., Kohno, K., et al. 2015, PASJ, 67, 8
Pan, Z., Li, D., Chang, Q., et al. 2017, ApJ, 836, 194
Pety, J., Teyssier, D., Fossé, D., et al. 2005, A&A, 435, 885
Pilleri, P., Treviño-Morales, S., Fuente, A., et al. 2013, A&A, 554, A87
Pilyugin, L. S., Vílchez, J. M., & Contini, T. 2004, A&A, 425, 849
Pilyugin, L. S., Thuan, T. X., & Vílchez, J. M. 2007, MNRAS, 376, 353
Priestley, F. D., Barlow, M. J., & Viti, S. 2017, MNRAS, 472, 4444
Röllig, M., Abel, N. P., Bell, T., et al. 2007, A&A, 467, 187
Rosenberg, M. J. F., Kazandjian, M. V., van der Werf, P. P., et al. 2014, A&A, 564, A126
Rosenberg, M. J. F., van der Werf, P. P., Aalto, S., et al. 2015, ApJ, 801, 72
San José-García, I., Mottram, J. C., van Dishoeck, E. F., et al. 2016, A&A, 585, A103
Schinnerer, E., Eckart, A., Tacconi, L. J., Genzel, R., & Downes, D. 2000, ApJ, 533, 850
Shirley, Y. L. 2015, PASP, 127, 299
Skrutskie, M. F., Cutri, R. M., Stiening, R., et al. 2006, AJ, 131, 1163
Sternberg, A., & Dalgarno, A. 1995, ApJS, 99, 565
Tacconi, L. J., Genzel, R., Blietz, M., et al. 1994, ApJ, 426, 77
Takano, S., Nakajima, T., Kohno, K., et al. 2014, PASJ, 66, 75
Tosaki, T., Kohno, K., Harada, N., et al. 2017, PASJ, 69, 18
Tucker, K. D., Kutner, M. L., & Thaddeus, P. 1974, ApJ, 193, L115
Turner, B. E., Terzieva, R., & Herbst, E. 1999, ApJ, 518, 699
Ulvestad, J. S., Neff, S. G., & Wilson, A. S. 1987, AJ, 93, 22
Usero, A., García-Burillo, S., Fuente, A., Martín-Pintado, J., & Rodríguez-Fernández, N. J. 2004, A&A, 419, 897
van Kempen, T. A., Kristensen, L. E., Herczeg, G. J., et al. 2010, A&A, 518, L121
Vasta, M., Barlow, M. J., Viti, S., Yates, J. A., & Bell, T. A. 2010, MNRAS, 404, 1910
Viti, S. 2017, A&A, 607, A118
Viti, S., Jimenez-Serra, I., Yates, J. A., et al. 2011, ApJ, 740, L3
Viti, S., García-Burillo, S., Fuente, A., et al. 2014, A&A, 570, A28
Walsh, A. J., Thorwirth, S., Beuther, H., & Burton, M. G. 2010, MNRAS, 404, 1396
Wang, M., Henkel, C., Chin, Y.-N., et al. 2004, A&A, 422, 883
Watt, G. D. 1983, MNRAS, 205, 321
Watt, G. D., White, G. J., Millar, T. J., & van Ardenne, A. 1988, A&A, 195, 257
Wilson, A. S., & Ulvestad, J. S. 1982, ApJ, 263, 576
Wilson, A. S., & Ulvestad, J. S. 1983, ApJ, 275, 8
Wilson, A. S., & Ulvestad, J. S. 1987, ApJ, 319, 105
Wootten, A., Bozyan, E. P., Garrett, D. B., Loren, R. B., & Snell, R. L. 1980, ApJ, 239, 844

[1] Observatorio Astronómico Nacional (OAN-IGN)-Observatorio de Madrid, Alfonso XII, 3, 28014 Madrid, Spain
e-mail: s.gburillo@oan.es
[2] Department of Physics and Astronomy, UCL, Gower Place, London WC1E 6BT, UK
[3] Observatoire de Paris, LERMA, CNRS, 61 Av. de l'Observatoire, 75014 Paris, France
[4] INAF–Osservatorio Astrofisico di Arcetri, Largo Enrico Fermi 5, 50125 Firenze, Italy
[5] Joint ALMA Observatory, Alonso de Córdova, 3107 Vitacura, 763-0355 Santiago, Chile
[6] ESO, Alonso de Córdova, 3107 Vitacura, 763-0355 Santiago, Chile
[7] Institut de Radio Astronomie Millimétrique (IRAM), 300 rue de la Piscine, Domaine Universitaire de Grenoble, 38406 St. Martin d'Hères, France
[8] Department of Earth and Space Sciences, Chalmers University of Technology, Onsala Observatory, 439 94 Onsala, Sweden
[9] Max-Planck-Institut für Radioastronomie, Auf dem Hügel 69, 53121 Bonn, Germany
[10] Instituto de Astrofísica de Canarias, Calle Vía Láctea, s/n, 38205 La Laguna, Tenerife, Spain
[11] Departamento de Astrofísica, Universidad de La Laguna, 38205, La Laguna, Tenerife, Spain
[12] Centro de Astrobiología (CSIC-INTA), ESAC Campus, 28692 Villanueva de la Cañada, Madrid, Spain
[13] Astronomy Department, King Abdulazizi University, PO Box 80203, 21589 Jeddah, Saudi Arabia
[14] European Southern Observatory (ESO), Karl-Schwarzschild-Strasse 2, 85748 Garching bei München, Germany
[15] Max-Planck-Institut für extraterrestrische Physik, Postfach 1312, 85741 Garching, Germany
[16] Leiden Observatory, Leiden University, PO Box 9513, 2300 RA Leiden, The Netherlands